Journal of Materials Chemistry A

PAPER

View Article Online
View Journal | View Issue

Cite this: J. Mater. Chem. A, 2014, 2, 19717

Oxygen transport kinetics of the misfit layered oxide $Ca_3Co_4O_{9+\delta}$†

V. Thoréton,[a] Y. Hu,[b] C. Pirovano,[a] E. Capoen,[a] N. Nuns,[a] A. S. Mamede,[a] G. Dezanneau,[b] C. Y. Yoo,[c] H. J. M. Bouwmeester[c] and R. N. Vannier*[a]

Received 2nd May 2014
Accepted 21st September 2014

DOI: 10.1039/c4ta02198c

www.rsc.org/MaterialsA

The oxygen transport kinetics of the misfit-layered cobaltite, $Ca_3Co_4O_{9+\delta}$, known for its thermoelectric properties, was investigated by combined application of $^{18}O/^{16}O$ isotope exchange and electrical conductivity relaxation techniques. Although oxygen diffusion is found to be two orders of magnitude lower than in well-investigated lanthanum nickelates, *e.g.*, $La_2NiO_{4+\delta}$, the mixed ionic–electronic conductor $Ca_3Co_4O_{9+\delta}$ is found to exhibit fast surface exchange kinetics ($k^* = 1.6 \times 10^{-7}$ cm s^{-1} at 700 °C to be compared to 1.3×10^{-7} cm s^{-1} for the nickelate), rendering it a promising electrode for application as an air electrode in solid oxide cells. In parallel, the chemical nature of the outermost surface of $Ca_3Co_4O_{9+\delta}$ was characterized by means of Low Energy Ion Scattering (LEIS) spectroscopy. The absence of cobalt at the sample's outermost surface suggests that the $Ca_2CoO_{3-\delta}$ rock salt layers in the structure may play a key role in the oxygen exchange mechanism.

1 Introduction

Chemical energy storage and efficient conversion of chemical energy into electricity represent one of the most important technological and scientific challenges for addressing the present and future energy requirements. In this field, reversible Solid Oxide Cells (SOCs) are promising. They can operate in a reversible mode, in both electrolyser (SOEC) and fuel cell (SOFC) modes, allowing storage of intermittent electricity from a wind or solar plant using hydrogen as a vector of energy. However, in such devices, the high operating temperatures (800–1000 °C) put very strict constraints on material selection, which results in high production costs and durability problems. These drawbacks constitute the principle obstacle for successful mass commercialisation, and current targets of cost and durability suppose the SOC devices to operate in the intermediate temperature range *i.e.* 600–750 °C. This has stimulated research on new SOFC cathodes, since the main limiting reaction in this electrochemical device is oxygen reduction. In this context, perovskite-structured cobaltites and ferrites are well known for their high mixed ionic–electronic conductivity, and high activity for the oxygen reduction reaction. Among these, $La_{0.6}Sr_{0.4}Co_{0.2}Fe_{0.8}O_{3-\delta}$ (LSCF) is one of the most well-studied cathode materials. However, a major drawback of these mixed conductors is their high thermal expansion coefficient, *e.g.* 14–15 $\times 10^{-6}$ K^{-1} for LSCF,[1] far higher than those of the commonly used electrolytes as yttria-stabilized zirconia (YSZ) (10×10^{-6} K^{-1}) and gadolinia-doped ceria (GCO) (12×10^{-6} K^{-1}).[2,3] Recently, promising electrochemical performances were shown at UCCS on the well-known thermoelectric $Ca_3Co_4O_{9+\delta}$ (CCO)[4–6] which due to its layered structure exhibits a thermal expansion coefficient of 9–10 $\times 10^{-6}$ K^{-1}, *i.e.*, in the same range as YSZ and GCO.[4]

For the 70 wt% CCO–30 wt% GCO composite electrode, an area specific resistance (ASR) of 1 Ω cm^2 was measured at 700 °C.[5] After optimisation of the composition and thickness, it could be further decreased to 0.5 Ω cm^2 at 700 °C for a 50 wt% CCO–50 wt% GCO composite electrode. In a recent study, this promising performance was confirmed by Samson *et al.*,[7] who reported a polarization resistance of 0.64 Ω cm^2 at 600 °C for the composite cathode consisting of 50 vol% CCO–50 vol% GCO, which corresponds to about 40 wt% CCO–60 wt% GCO. In addition, using a samaria-doped ceria electrolyte, Zou *et al.*[8] measured a maximum power density of 430 mW cm^{-2} at 700 °C for a 70 wt% $Ca_{2.9}Bi_{0.1}Co_4O_{9+\delta}$–30 wt% $Ce_{1.8}Sm_{0.2}O_{1.95}$|$Ce_{1.8}Sm_{0.2}O_{1.95}$|$Ce_{1.8}Sm_{0.2}O_{1.95}$–Ni button cell.

It is worth noting that CCO and the La-doped analogue $Ca_{2.7}La_{0.3}Co_4O_{9+\delta}$ were also tested as a cathode for the proton conducting SOFC with $BaCe_{0.9}Y_{0.1}O_{3-\delta}$ as the electrolyte. Using

[a]Univ Lille Nord de France, CNRS UMR 8181, Unité de Catalyse et de Chimie du Solide – UCCS, ENSCL, Université Lille 1, CS 90108, 59652 Villeneuve d'Ascq Cedex, France. E-mail: rose-noelle.vannier@ensc-lille.fr; Fax: +33 (0)320436814; Tel: +33 (0) 320436583

[b]Laboratoire Structures, Propriétés et Modélisation des Solides (SPMS), Ecole Centrale Paris, Grande Voie des Vignes, 92295 Châtenay-Malabry, France

[c]Inorganic Membranes, Faculty of Science and Technology, MESA+ Institute for Nanotechnology, University of Twente, P.O. Box 217, 7500 AE, Enschede, The Netherlands

† Electronic supplementary information (ESI) available: Details on SIMS analysis, ionic cartography of a CCO sample and the corresponding line scan, cartography of the total ionic signal collected on a slice of CCO pellet, X-ray diffraction at varying temperatures and oxygen partial pressure with corresponding unit-cell parameter evolution, CCO TGA analysis at varying temperatures and oxygen partial pressures, LEIS analysis on a CCO thin film prepared by PLD, and D_{chem} and k_s (PIE) values. See DOI: 10.1039/c4ta02198c

the pure electrode material, an ASR of 2.2 Ω cm^2 was obtained at 600 °C.[9]

As a thermoelectric material, CCO exhibits a high electrical conductivity with values above 100 S cm^{-1} between room temperature and 800 °C. It exhibits almost the same conductivity at room temperature with a metallic to semiconducting transition around 275 °C.[10] It adopts a misfit structure, consisting of alternating "hexagonal" CoO_2 layers of CdI_2 type and $Ca_2CoO_{3-\delta}$ rock salt layers as shown in Fig. 1. It can be described in the 5D space group $C2/m(1\delta0)(\alpha0\gamma)gm$.[11] Alternatively, the structure can be viewed as made of two lattices, with common a and c cell parameters, and with a different periodicity along the [010] direction (modulation vector $q = b_{RS}/b_H = 1.62$). The correct formula of CCO in fact is $[Ca_2CoO_{3-\delta'}][CoO_2]_{1.62}$.

All cobalt valences Co(II), Co(III) and Co(IV) are present. With oxygen vacancies located in the central layer of the rock salt subsystem,[12] oxide ion diffusion is expected in these layers, but has not been demonstrated yet. Moreover, since Co(III) is known to be particularly active for the reduction of oxygen molecules into oxide ions, good kinetics of oxygen exchange at the surface of these compounds is expected.[13]

In this field, isotope exchange and relaxation methods are usually applied for the assessment of relevant parameters associated with the surface exchange kinetics and diffusion of oxide ions in the bulk.[14,15]

The principle of IEDP (Isotope Exchange Depth Profiling) relies on the measurement of the ^{18}O diffusion profile in a dense ceramic after annealing in an ^{18}O enriched atmosphere for a given time. Oxygen self-diffusion tracer (D^*, cm^2 s^{-1}) and surface exchange coefficients (k^*, cm s^{-1}) were determined by fitting the experimental data measured by Secondary Ion Mass Spectrometry (SIMS) to the Fick's diffusion laws using the solution given by Crank for diffusion in a semi-infinite media with evaporation from the solid state:[16]

$$C'(x,t) = \frac{C(x,t) - C_{bg}}{C_g - C_{bg}} = \mathrm{erfc}\left[\left(\frac{x}{2\times\sqrt{D^*\times t}}\right)\right] - \left[\exp\left(\frac{k^*x}{D^*} + \frac{k^{*2}t}{D^*}\right) \times \mathrm{erfc}\left(\frac{x}{2\times\sqrt{D^*\times t}} + k^*\sqrt{\frac{t}{D^*}}\right)\right] \quad (1)$$

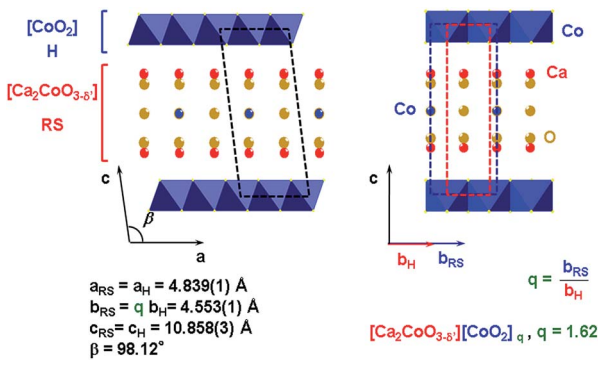

Fig. 1 $Ca_3Co_4O_{9+\delta}$ (CCO) structure consisting of alternating CoO_2 layers and $Ca_2CoO_{3-\delta}$ rock salt layers.

where C_{bg} is the natural ^{18}O ratio, C_g is the ^{18}O ratio in the enriched exchange atmosphere, D^* is the ^{18}O diffusion coefficient, k^* is the surface exchange coefficient, and t is the diffusion time.

In contrast to IEDP, Electrical Conductivity Relaxation (ECR) is a non-equilibrium method, and commonly applied to study oxygen transport kinetics of mixed ionic–electronic conductors. The method is based on measurement of the transient conductivity after a step-wise change in the ambient pO_2, assuming a linear relationship between oxygen stoichiometry and conductivity of the sample. D_{chem} and k_{chem} obtained from experiments can be related to D^* and k^*, respectively, *via* the thermodynamic factor, γ. The latter can be calculated from the data of oxygen stoichiometry,

$$D_{chem} = \gamma D^*$$

$$k_{chem} = \gamma k^*$$

$$\gamma = 1/2\frac{\mathrm{dln}\, pO_2}{\mathrm{dln}\, c_O} \approx 1/2\frac{\Delta \mathrm{ln}\, pO_2}{\Delta \mathrm{ln}\, c_O} \quad \text{when } \sigma_e \gg \sigma_i \quad (2)$$

where $\Delta \ln pO_2$ and $\Delta \ln c_O$ are the corresponding variations in the oxygen partial pressure and oxygen content, and σ_e and σ_i, are the electronic and ionic conductivity, respectively.

A major drawback of IEDP and ECR is that both techniques require ceramics with a relative density higher than 95%, ideally more than 98%. For the characterisation of surface kinetics, the Pulse ^{18}O–^{16}O Isotopic Exchange (PIE) technique, recently introduced by Bouwmeester *et al.*,[17,18] has the advantage to be applied on oxide powders. During the experiment, the powder is loaded in a packed-bed micro-reactor and allowed to equilibrate at a chosen oxygen partial pressure and temperature for a selected time. By maintaining the conditions of chemical equilibrium, the response to an ^{18}O enriched pulse fed through the reactor under continuous flow conditions is measured by mass spectrometric analysis of the gas phase fractions of oxygen isotopomers ($^{18}O_2$, $^{16}O^{18}O$ and $^{16}O_2$) at the exit of the reactor. The exchange rate $\Re_0$ (mol O m^{-2} s^{-1}) is calculated from the mean residence time and uptake of ^{18}O by the sample with a known surface area. Mass balance analysis yields a simple explicit equation for the surface exchange rate:

$$\Re_0 = \frac{n}{\tau_r S}\ln\left(\frac{f_g^{18}}{f_{ge}^{18}}\right) \quad (3)$$

where f_{gi}^{18} and f_{ge}^{18} are the ^{18}O isotope fractions in the pulse volume at the inlet and the exit of the reactor, respectively, τ_r is the average residence time of the reactor, n is the total number of oxygen atoms in the gas phase and S is the oxide surface area available for the exchange for the entire packed bed reactor. The relationship between $\Re_0$ and k^* is given by:

$$\Re_0 = k^* c_O \quad (4)$$

where c_O is the oxygen concentration in the solid.

It is also worth noting that the surface exchange kinetics is highly dependent on the chemistry of the oxide surface and therefore the nature of the outermost atoms at the surface of the solid oxide. A unique technique to answer this question is Low-Energy Ion Scattering spectroscopy (LEIS) (for a recent review on this technique, see ref. 19).

In the present study, for the first time, $^{18}O/^{16}O$ IEDP, ECR and PIE techniques were applied to investigate the oxygen transport properties of CCO. LEIS was applied to study its oxide surface chemistry in order to gain more insights into the surface exchange mechanism of this material.

2 Experimental

The powder of CCO was prepared by solid-state reaction from $CaCO_3$ (Prolabo, 99.5%, kept at 100 °C to avoid moisture) and Co_3O_4 (Alfa Aesar, 99.7%). To increase the reactivity, stoichiometric amounts of the precursor materials were first attrition milled for 3 hours (Netzch PE 075, 1000 rpm) in ethanol using zirconia balls (2 mm diameter) and, then annealed three times at 900 °C with intermediate grindings. The starting materials and final products were analysed by X-ray diffraction, using a D8 advance Bruker AXS diffractometer equipped with a Cu anode (CuK_α) and a 1D LynxEye PSD detector and an Energy Dispersive Spectrophotometer attached to a SEM (Hitachi S4700). The Fullprof software [v2.05, July 2011] was used for refinement of the unit cell parameters of CCO.[20] For the refinement, the CCO phase was considered as a two phase-(H) and (RS) layer mixture with common a, c and β cell parameters, constrained to be the same, and different b_H and b_{RS}, refined independently. An Accupyc II 1340 Micromeritic pychnometer was used to measure the powder density. The specific surface area of the powder was measured by the BET method, using a Micromeritics Gemeni VII apparatus.

Thermal analysis was conducted in air, using a TG/DTA Setaram Setsys apparatus. 40 mg of the sample powder was introduced into a Pt crucible, and the experiment was carried out at a heating rate of 0.5 °C min^{-1} under air flow (0.4 L h^{-1}) from room temperature to 950 °C. A blank experiment with an empty crucible was performed to correct the data for effects of buoyancy. The absolute oxygen stoichiometry of the sample was determined by iodometric titration.[21] Thermogravimetry was also carried out for evaluation of the oxygen stoichiometry of the sample as a function of pO_2. In this case, a Setaram 92-1750 apparatus was used. The experiment was carried out using 50 mg of powder in a Pt crucible under a flowing O_2–N_2 mixture (5 L h^{-1}), with three successive oxygen partial pressures (100, 200 and 400 mbar), and temperature ranging from 600 to 750 °C (50 °C step) for each pressure. For this set-up, the buoyancy was negligible and the data were directly used to derive the thermodynamic factor at each temperature.

A D8 advance Bruker AXS diffractometer equipped with an Anton Paar HTK 1200N high temperature chamber, a 1D VÅNTEC-1 detector and a Cu anode (CuK_α) was used for powder X-ray diffraction at different temperatures. A diffractogram was recorded with 25 °C intervals from room temperature to 950 °C in the 7–65° 2θ range with a 0.022° step and a counting time of 1 s per step on heating, and every 50 °C on cooling. The sample was deposited on a gold sheet to protect it from the alumina sample holder. Additional experiments were carried out under the same conditions at variable oxygen partial pressures at 700 °C under a gas flow of 6 L h^{-1}. A mixture of oxygen and nitrogen was used to vary the oxygen partial pressure from 10^{-5} to 1 bar. For this study the data collection was limited to the 22–47° 2θ range, and the counting time was raised to 2 s per step. To ensure thermodynamic equilibrium was reached, four successive diffractograms were recorded for each oxygen partial pressure.

Dense ceramics were prepared by spark plasma sintering (SPS) on the National Platform in Toulouse (France). A carbon die of 15 mm in diameter was used. Samples with a relative density higher than 98% were obtained in 15 min with a 2 min dwell, at 850 °C, under a 50 MPa (8.8 kN) pressure. To remove carbon residues, the pellets were polished with SiC paper and annealed for 12 h at 800 °C. The sample morphology was investigated by scanning electron microscopy (SEM), using a Hitachi S-3400N.

IEDP, ECR and PIE techniques were used to measure the surface exchange and diffusion properties of CCO.

IEDP samples were prepared from SPS dense ceramics annealed at 900 °C for 72 hours. Their surfaces were polished with SiC papers and diamond sprays to 1/4th of a micron. The roughness of the sample and the crater depth were measured post-analysis with a KLA Tencor Alpha-step IQ profilometer. The $^{18}O/^{16}O$ isotope exchange annealing was carried out on pre-annealed dense samples in the 500–753 °C range (see Table 1 for experimental details), using the exchange rig newly installed at UCCS. To quantify the ^{18}O isotope concentration in the exchange atmosphere, a silicon wafer was annealed at 1000 °C under 200 mbar of the ^{18}O enriched oxygen for more than 12 hours. In detail, for each experiment, the sample was introduced in a quartz tube and preannealed under normal oxygen (research grade oxygen 99.995% ALPHAGAZ™ 1 of normal isotopic abundance) for at least 12 hours to get the thermodynamic equilibrium. Then, it was quenched. Normal oxygen was pumped out and ^{18}O enriched oxygen was introduced into the tube before rolling on the pre-heated furnace to carry out the isotopic exchange for a given annealing time. The temperature of the sample was controlled thanks to a thermocouple placed

Table 1 Conditions of $^{18}O/^{16}O$ isotope exchange

Temperature (°C)	Pressure (mbar)	Pre-annealing time (hours)	Annealing time (min)	^{18}O ratio in the gas phase
597	226	60	718	0.82
653	209	144	612	0.73
707	230	12	59	0.84
701	232	60	390	0.82
700[a]	230	60	390	0.26
702	1000	12	65	0.89
753	232	20	238	0.84

[a] This experiment was carried out on the exchange rig available at Imperial College London.

at the vicinity of the sample but outside the quartz tube to avoid any artefact with the gas phase.

In this study, the depth profile[22] on the sample surface and line-scan[14] analyses were carried out. In this latter case, slices of the sample were cut perpendicular to its surface. Two of them were placed side to side (see Fig. S1 in the ESI†) to avoid edge effects of the sample. The cross-section was polished to 1/4th of a micron prior to the SIMS analysis. A TOF.SIMS^5 machine (ION-TOF), equipped with a bismuth gun for analysis and a caesium gun for sputtering, was used to measure the oxygen isotope depth profile in the sample. The pressure in the chamber was maintained below 5×10^{-8} mbar during operation. Negative secondary ions were collected. Most of the time, experiments were carried out with a Bi^+ beam. Mainly burst mode was used for depth profile analysis. For line scan, because of the need for resolution, only the 8 pulse burst mode analysis was carried out, applying Poisson correction. In depth profile mode analysis, the bismuth ion beam rastered over 100 μm × 100 μm and the 2 keV Cs^+ ion beam rastered over 300 μm × 300 μm for sputtering. In the case of line scan mode analysis, the bismuth ion beam rastered over 100 μm × 100 μm or 300 μm × 300 μm depending on the depth penetration length and the 0.5 to 2 keV Cs^+ ion beam rastered over 300 μm × 300 μm or 500 μm × 500 μm for sputtering. In both cases, the no-interlaced analysis was used. To derive the line scan, the images were integrated along the diffusion axis (see the ESI† for more details on the SIMS analysis).

The surface of the samples was characterized by FTIR on a Bruker vertex 70 spectrometer coupled to a Hyperion 3000 microscope and Raman scattering at room temperature with the 647.1 nm excitation line of a Spectra Physics krypton ion laser.

ECR experiments were performed in the 650–750 °C range, switching alternately the oxygen partial pressure in between 1.0 and 0.05 atm (argon–oxygen mix). Rectangular samples, 15 mm in length, 1 and 2 mm in width, were cut from the dense CCO pellets with a diamond saw, and their faces polished to 1/4th of micron. Conductivity measurements were performed using a four-probe configuration. Gold contacts were deposited on both sides of the sample. Once the sample was at equilibrium at a given temperature, the pO_2 was step-wise changed and the conductivity was monitored as a function of time.

Conductivity was measured at 1 kHz using a Keithley 6221 AC current source (i_{AC} = 1 mA) coupled to SRS830 Lock-in amplifier to measure the voltage drop at the same frequency. Experimental data were fitted using the theoretical model shown in ref. 15.

PIE experiments were carried out using a continuous flow (0.21 atm oxygen partial pressure) packed-bed micro-reactor as described in ref. 18. The temperature range was 500 to 750 °C (50 °C step). About 40 mg of powder was introduced in between two quartz wool plugs in the centre of the quartz tubular micro-reactor of 2 mm inner diameter, and placed in a tubular furnace. The $^{16}O_2$–Ar gas mixture was used as the carrier gas with a 50 mL min^{-1} (STP) flow rate. The response to the $^{18}O_2$–N_2 pulse (500 μL) with the same oxygen partial pressure as the carrier gas, was passed through the reactor, and the effluent pulse was analysed by using an online mass spectrometer (Omni Star TM GSD 301 Pfeifer-Vaccum) at the exit of the reactor. For each measurement, the sample was allowed to equilibrate for 30 minutes at the required temperature. Three pulses of labelled oxygen were delivered successively at the reactor inlet to a six channel valves. Masses of $^{16}O_2$, $^{16}O^{18}O$ and $^{18}O_2$ isotopomers were recorded and N_2 was used for normalisation.

LEIS measurements were performed on the powder and a dense SPS ceramic using a Qtac^{100} (ION-TOF) instrument. Both powder and ceramic were heat treated at 800 °C just before the LEIS analysis. This was performed under static air in a separate furnace, prior to loading the sample into the instrument. The powder was manually pressed in a 10 mm (diameter) die. Before insertion in the analysis chamber, samples were submitted to a beam of neutral atomic oxygen (2–3 × 10^{-4} mbar) to remove possible organic contamination. A $^4He^+$ (3 keV, 5 nA) beam was used for the analysis. For the powder, in a first step, 105 spectra were recorded for 120 seconds on a surface of 1 mm^2, and then, using the same beam, 45 spectra were recorded on a reduced surface of 0.57 mm^2 for the same time. It was estimated that 16 monolayers had been removed after the final spectrum. For the dense ceramic, the analysis was carried out on a 1 mm^2 surface; to go deeper in the sample, a 8 keV to 450 nA $^{20}Ne^+$ beam was used for sputtering. In this case the spectra were recorded for 60 seconds and the estimated removed depth was 240 monolayers after the last spectrum.

To verify the presence of sodium on the sample surface and possibility of potassium which could interfere with calcium for LEIS analysis, Electron Probe Microanalysis (EPMA) was also carried out on a dense ceramic sample after ^{18}O exchange. The analysis was carried out on a Cameca SX 100 apparatus on both a "depth profile" sample to analyse the sample surface and a "line scan" sample to get information on the bulk of the sample.

3 Results and discussion

Characterization of the powder and ceramics

The powder purity was confirmed by X-ray diffraction and EDS analysis. No zirconium contamination from attrition milling was detected. Unit cell parameters refined by full pattern matching are summarized in Table 2.

These are found in good agreement with those reported previously for CCO.[11] From iodometric titration, a mean cobalt valence of 3.18(5) was deduced, leading to a vacancy fraction (δ')

Table 2 Unit cell parameters of CCO from XRD on the powder and sintered ceramics

	Powder	Dense ceramics
a (Å)	4.8301(2)	4.8345(8)
b_H (Å)	2.8228(2)	2.819(2)
b_{RS} (Å)	4.5580(3)	4.543(2)
c (Å)	10.8416(7)	10.852(2)
β (°)	98.129(4)	98.14(2)
b_{RS}/b_H	1.6149(3)	1.611(2)

equal to 0.06(1) in the rock salt layers. The measured density (4.66(4) g cm^{-3}) was found in good agreement with the calculated one (4.68(3) g cm^{-3}). The specific surface area of the powder was 0.251 m^2 g^{-1}, indicating a rather coarse grain size.

Data of TG/TDA analysis of the CCO powder are shown in Fig. 2. DTA reveals three reversible phenomena, which are endothermic on heating and exothermic on cooling. The first transition at 130 °C was attributed to a disorder–order transition to a more regular configuration of the cobalt ions in the rock salt layers at high temperature compared to room temperature, related to a rearrangement of the central [CoO] layer of the [$Ca_2CoO_{3-\delta'}$] layers.[11] At a similar temperature Masset *et al.*[23] observed anomalies in the magnetic susceptibility and electrical resistivity. The second transition, at 550 °C, is accompanied by a change in the rate of mass-loss. The temperature at which the transition occurs can be associated with a magnetic transition in CCO as reported in ref. 24. At 950 °C, the phase decomposes into $Ca_3Co_2O_6$ and CoO, but the transformation is reversible as confirmed by X-ray diffraction at different temperatures (see Fig. S2 and S3 in the ESI†).

This compound was also studied at 700 °C under different oxygen partial pressures. It was stable from 1 bar to 50 mbar of oxygen, but decomposes under a nitrogen atmosphere (pO_2 < 10^{-2} mbar) into calcium oxide and cobalt oxide. Interestingly, the transformation was reversible (see Fig. S4 and S5 in the ESI†).

From the evolution of the mass-loss in function of the temperature for different oxygen partial pressures (see Fig. S6 in the ESI†), the variation of total oxygen stoichiometry was deduced. The values are summarized in Table 3 and were used to derive the thermodynamic coefficient, γ.

After spark plasma sintering, ceramics with a relative density higher than 98% were obtained. A SEM image of the surface of a ceramic is shown in Fig. 3. It confirmed the high density of the sample, showing evidence of faceted and elongated grains.

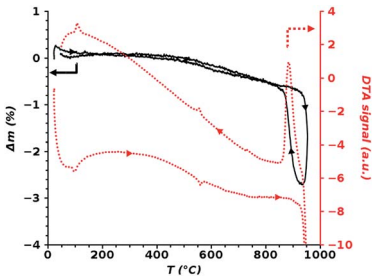

Fig. 2 TG/DTA analysis of the CCO powder, collected at heating and cooling rates of 5 °C min^{-1} under flowing air.

Table 3 CCO total oxygen stoichiometry derived from TGA analysis as a function of temperature and oxygen partial pressure (to be compared to 9.18 measured at room temperature under 200 mbar measured by iodometry)

Temp. (°C)	δ at 100 mbar	δ at 200 mbar	δ at 400 mbar	γ
650	9.12	9.13	9.14	232
700	9.10	9.12	9.13	212
750	9.08	9.10	9.11	199

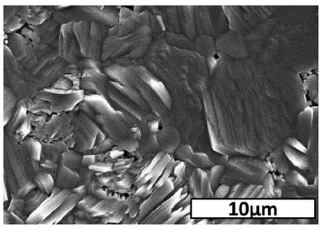

Fig. 3 SEM micrograph of a CCO ceramic after SPS and preannealing.

$^{18}O/^{16}O$ isotope exchange

A dramatic evolution of the surface roughness of the polished dense ceramic samples was noticed when they were directly annealed at the exchange temperature: when the sample was annealed for 12 hours at 900 °C and then polished to 1/4th of micron prior to the exchange, the initial roughness (R_a) of 17–25 nm increased to a reasonable mean value of 55 nm after annealing at 600 °C for 60 hours under 200 mbar of oxygen against 500 nm without preannealing. This was likely due to spark plasma sintering which can produce stress inhomogeneities.[25] Therefore, samples were annealed at 900 °C for 72 hours under static air in a muffle furnace to release the surface constrains before polishing their surfaces and carrying out the isotope exchange in a quartz tube.

The evolution of the isotope fraction as a function of depth measured on the sample annealed at 701 °C under 232 mbar of oxygen for 390 minutes is given in Fig. 4. Both data recorded in depth profile and line scan mode are reported. A good junction between the two sets of data is observed. The evolution of the isotopic fraction is in good agreement with the expected one, except at the vicinity of the sample's surface where a decrease of the isotopic fraction is noticed along 1 to 2 µm. As a matter of comparison, the same experiment was carried out on the rig available at Imperial College London. The same behaviour was

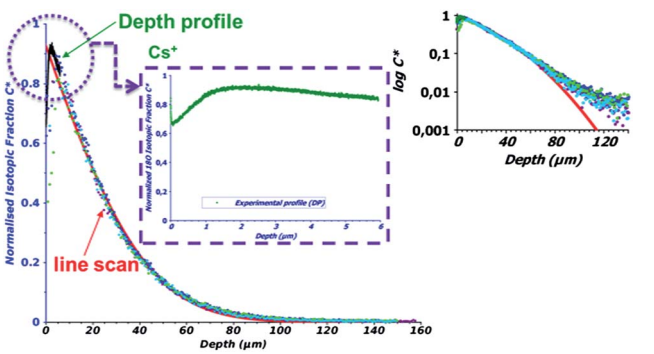

Fig. 4 Normalised ^{18}O diffusion profile on CCO after diffusion for 390 min at 701 °C under 230 mbar of dry ^{18}O oxygen. A focus on the isotopic fraction near the ceramic surface is shown in the inset. The profile is also given in a logarithm scale which shows evidence of a lack of agreement for depth higher than 70 µm which may be due to fast grain boundary transport or due to anisotropic diffusion.

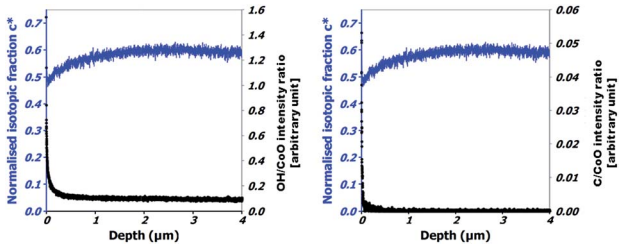

Fig. 5 Evolution of OH (left) and C (right) signals at the surface (normalised to CoO). O stands for ^{16}O and ^{18}O. The normalised oxygen isotopic fraction $^{18}O/(^{18}O + {}^{16}O)$ is given in blue for comparison.

observed and confirmed for all samples. The possibility of a decrease of ^{18}O in the gas phase was ruled out, since the variation of ^{18}O in the gas phase was estimated at 2% maximum taking into account the volume of the tube used for the exchange and by integrating the diffusion profile on the whole surface of the pellet to derive the amount of ^{18}O in the ceramic.

The possibility of oxygen diffusion at room temperature was also excluded by a second analysis of one sample, one year later. However, higher concentrations of carbon and hydroxyl were noticed at the near surface and one cannot exclude carbonation or hydroxylation but these phenomena were only observed along 100 to 200 nm depth, a shorter depth than ^{18}O surface depletion as shown in Fig. 5. To confirm the presence of a carbonate or hydroxyl group, FTIR and Raman spectroscopy were carried out but led to no clear evidence of these two species. Therefore, only the data 2 μm far from the sample surface were used for the fitting of the experimental data to eqn (1).

In the inset of Fig. 4, the profile was drawn in the log scale to compare the experimental data and the fitted curve in the high depth part of the profile. A ⟪tail⟫ was noticed, suggesting the occurrence of a second diffusion mechanism. This could be attributed either to fast grain boundary transport or to anisotropic diffusion. Considering the large grain size and the inherent anisotropy of the material, a deeper examination was currently carried out on fully textured samples.

The derived k^* and D^* parameters are summarized in Table 4. The extrapolated normalised isotopic fraction at the surface, C_0, an additional parameter $\eta = k\sqrt{\frac{t}{D^*}}$ and the diffusion length $2\sqrt{D^*t}$ are also given. A C_0 value close to 1 and a η value higher than 10 indicate high surface kinetics compared to oxide ion diffusion. In this case, confidence in D^* is high but in k^* is low. Conversely, when C_0 is far lower than unity and η is lower than 0.1, the confidence in k^* is high and low for D^*.[26] At 700 °C, three different samples were characterized. Whereas close D^* values were obtained, a larger k value was derived for the sample annealed at 701 °C with a higher C_0 value, indicative of a lack of accuracy for the k value. With a C_0 of 0.68 and a η of 1.5, the sample exchanged in London is the most reliable and one can consider that the surface exchange coefficient is equal 1.6×10^{-7} cm s^{-1} and the coefficient of diffusion is equal to 2.7×10^{-10} cm s^{-2} at 700 °C under 230 mbar. In good agreement with thermal activation, an increase of both parameters with temperature increase is observed. In contrast, the diffusion coefficient is slightly decreased when the oxygen partial pressure increases from 230 mbar to 1 bar, likely due to a filling of oxygen vacancy as shown by X-ray diffraction.

ECR and PIE

To confirm these data, samples were also characterized by ECR and PIE. The evolution of the electrical conductivity as a function of time recorded at 700 °C is shown in Fig. 6 and the corresponding D_{chem} is given in Table S1 in the ESI.†

A good reversibility between oxidation and reduction was observed. Under these conditions, only the diffusion coefficient could be derived with precision, reflecting a D_{chem}/k_{chem} characteristic length much smaller than the size of the sample.

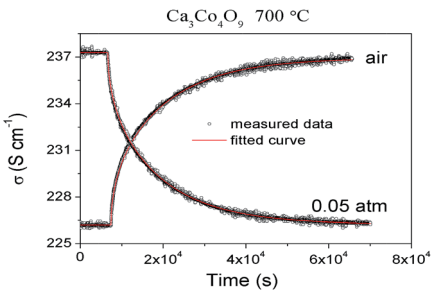

Fig. 6 Conductivity relaxation measured on CCO at 700 °C and corresponding modelling. A good reversibility between oxidation and reduction was observed.

Table 4 CCO transport parameters measured at several temperatures and oxygen partial pressures

Temperature (°C)	Pressure (mbar)	k^* (cm s^{-1})	D^* (cm^2 s^{-1})	$2\sqrt{D^*t}$ (μm)	$\eta = k\sqrt{\frac{t}{D^*}}$	C_0 (extrapolated)
597	226	3.3×10^{-8}	9×10^{-11}	39	0.52	0.48
653	209	8.0×10^{-8}	3.0×10^{-10}	66	0.78	0.54
707	230	1.6×10^{-7}	3.5×10^{-10}	22	0.50	0.39
701	232	8.0×10^{-7}	2.7×10^{-10}	50	7.0	0.92
700[a]	230	1.6×10^{-7}	2.7×10^{-10}	50	1.50	0.68
702	1000	1.5×10^{-7}	1.5×10^{-10}	15	0.77	0.5
753	232	5.0×10^{-6}	6.5×10^{-10}	61	23	0.98

[a] This experiment was carried out on the exchange rig available at Imperial College London.

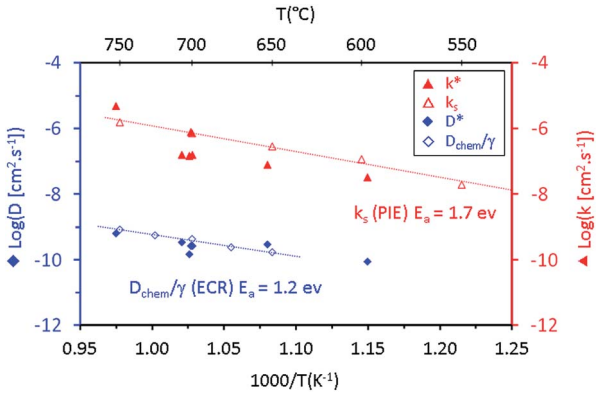

Fig. 7 Arrhenius plot of the transport coefficients k^* (cm s^{-1}) (triangles) and D^* (cm^2 s^{-1}) (squares). Values obtained by IEDP (plain shapes) are compared to those obtained by ECR ($D^*_{chem} = D_{chem}/\gamma$) and PIE ($k_s$) (empty shapes). Activation energies from linear regressions (dotted lines) were derived for D^*_{chem} and k_s (respectively 1.2 and 1.7 eV).

Table 5 CCO transport parameters compared to the most promising SOFC cathode materials

	Temp/°C	P/mbar	k^*/cm s^{-1}	D^*/cm^2 s^{-1}
$Ca_3Co_4O_{9+\delta}$	700	230	1.6×10^{-7}	2.7×10^{-10}
$La_2NiO_{4+\delta}$ (ref. 27)	700	200	1.3×10^{-7}	1.6×10^{-8}
$La_{0.6}Sr_{0.4}CoO_{3-\delta}$ (ref. 28)	680	230	1.1×10^{-6}	2.0×10^{-8}
$GdBaCo_2O_{5+\delta}$ (ref. 29)	686	200	1.3×10^{-7}	1.3×10^{-9}

Taking into account the thermodynamic coefficients deduced from TGA analysis, at 650, 700 and 750 °C, these values are in good agreement with the data measured by IEDP (see Fig. 7). The derived k_s values obtained by PIE are also reported in Fig. 7. They are in the same order of magnitude but slightly higher than the data obtained by IEDP (values obtained by PIE are compared to values obtained by IEDP in Table S2 in the ESI†). These slightly higher values could not only be explained by a lower accuracy for IEDP data but also by different sample and grain anisotropies.

Activation energies of 1.2 eV and 1.7 eV were derived for D^*_{ECR} and k_s, respectively.

All these data confirm that CCO is a Mixed Ionic Electronic Conductor. When compared with the mass transport parameters of the most promising SOFC cathodes (see Table 5), CCO exhibits lower oxide ion diffusion which confirms the need for adding an oxide ion conductor to improve its electrochemical performances but its kinetics towards the oxygen reduction reaction are in the same order of magnitude of the best electrode materials studied at the moment. This, in addition to its thermal expansion coefficient in good agreement with YSZ and CGO ones, makes it a promising cathode material for SOFC.

LEIS

LEIS is a unique technique used to characterize the uppermost atomic layer of a solid. The initial and final spectra, recorded with a 3 keV $^4He^+$ beam, on a CCO powder and on a dense sample are shown in Fig. 8.

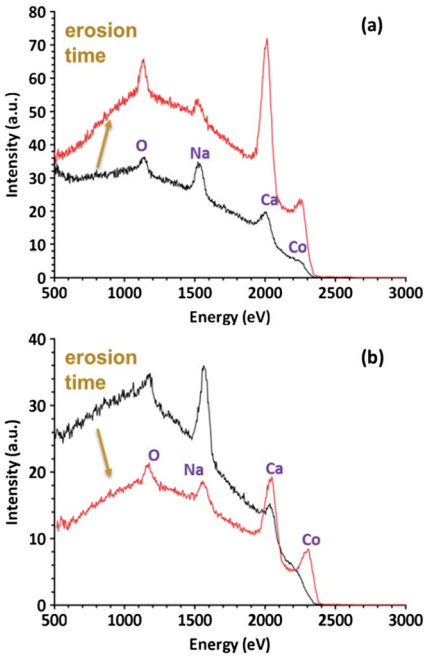

Fig. 8 Comparison of the ^4He (3 kV) LEIS spectra of the surface (21% of a monolayer) for both the powder (a) and dense ceramics (b). Spectra recorded after sputtering of the surface are also shown (about 16 and 240 monolayers below for powder and ceramic, respectively). In both cases, calcium atoms are at the outermost surface of samples.

For both samples, in addition to calcium, cobalt and oxygen, sodium was shown at the sample surface. The intensity of the peak decreased with sputtering time.

To confirm the possibility of sodium at the surface, EPMA was carried out on a dense ceramic after ^{18}O exchange on both the sample surface (analysis of a "depth profile" sample and in the bulk, analysis of a "line scan sample"). The presence of sodium at the surface was confirmed with a concentration of 0.2 wt%; it was lower than 0.02 wt% in the bulk which may indicate the presence of sodium as an impurity in the powder which likely segregates to the surface during annealing. Sodium segregation at the surface may impact the oxygen transfer as shown for YSZ for which oxygen exchange was considerably reduced when the surface was completely covered with oxide impurities.[30] It is worth noting that no potassium, which may interfere with calcium during LEIS analysis, was observed. Interestingly, calcium atoms were also shown at the outermost surface with only a shoulder for cobalt indicating its presence underneath the first atomic layer. The presence of Ca at the outermost surface with cobalt underneath the first layer of atoms was also confirmed on a CCO thin film prepared by pulse laser deposition for which no sodium contamination was observed (see Fig. S9 in the ESI†).

In the study of $SmCoO_3$, Fullarton *et al.* also demonstrated that samarium was found preferentially at the surface with only 5% of cobalt at the outmost surface and a segregation of strontium at the surface was shown for strontium doped compounds.[31]

Similarly, Viitanen *et al.* showed the absence of cobalt and iron in the outermost atomic layer of a $La_{0.6}Sr_{0.4}Co_{0.2}Fe_{0.8}O_3$ membrane.[32] Since the structure of CCO is a misfit of CoO_2 hexagonal layers and $Ca_2CoO_{3-\delta}$ rock salt layers, the presence of calcium at the surface would indicate that the surface of the solid is mainly made of rock salt layers. It is therefore likely that oxygen molecules dissociate at the surface of these rock salt layers with Ca–O at the outermost surface and, then, oxide ions diffuse in these layers through an oxygen vacancy diffusion mechanism. Conduction in the rock salt layers would be in good agreement with the high disorder of the Co–O layers within the rock salt layers as shown by Muguerra *et al.*[11]

4 Conclusions

Combining isotope exchange and conductivity relaxation techniques, we confirmed that $Ca_3Co_4O_{9+\delta}$, well-known for its thermoelectric behaviour, is a mixed ionic electronic conductor. Because of moderate oxygen diffusivity (2.7×10^{-10} cm^2 s^{-1} at 700 °C), this compound has to be used in a composite with an ionic conductor as a SOFC cathode. However, good exchange kinetics were shown with the oxygen surface exchange coefficient comparable to other cathode materials. It is similar to the well-known La_2NiO_4 cathode with the advantage of a low thermal expansion coefficient compared to other cobaltites, making this material a promising air electrode for solid oxide cells.

The structure of $Ca_3Co_4O_{9+\delta}$ is a misfit of CoO_2 layers of CdI_2 type and $Ca_2CoO_{3-\delta'}$ layers of rock salt type. Interestingly, despite sodium segregation, LEIS revealed mainly calcium at the outermost surface of the solid which indicates that $Ca_2CoO_{3-\delta'}$ layers are at the outermost surface of the solid and the oxygen reduction reaction occurs at the surface of these rock salt layers in which diffusion is facilitated thanks to oxygen vacancy and disorder in the Co–O layers sandwiched between 2 Ca–O layers. A 2D oxygen diffusion is therefore expected in this compound. A deeper insight into fully textured samples (single crystal or SPT ceramics) is in progress to characterise completely the foreseen diffusion anisotropy. Finally, since $Ca_3Co_4O_{9+\delta}$ compounds present an exchange coefficient comparable to that of cathode materials, improvements should focus on increasing the oxygen ion diffusion coefficients by doping on the calcium site for instance. The impact of impurities on oxygen exchange at the sample surface will also be studied.

Acknowledgements

The "Fonds Européen de Développement Régional (FEDER)", "CNRS", "Région Nord Pas-de-Calais" and French "Ministère de l'Education Nationale de l'Enseignement Supérieur et de la Recherche" are acknowledged for the funding of X-ray, EPMA and surface analyses facilities. V.T. is grateful to the University Lille 1 for funding his PhD grant. The authors are also grateful to the Agence Nationale de la Recherche for funding the ANR EVEREST (ANR-07-PANH-005) and IDEA-MAT (ANR-12-BS08-0012-01) projects. Patrick Rozier from CERIMAT is gratefully acknowledged for providing dense CCO pellets. Dr Helena Tellez-Lozano from Imperial College London is acknowledged for carrying a parallel exchange on the $^{18}O/^{16}O$ exchange rig available at Imperial College London. Maxence Vandewalle, Nora Djelal and Laurence Burylo from the UCCS are acknowledged for SEM and TG-DTA analyses and conventional XRD experiments, respectively. Séverine Bellayer from ENSCL is acknowledged for EPMA. Isabelle De Waele from LASIR is thanked for IR spectroscopy studies and Annick Rubbens from UCCS is thanked for Raman spectroscopy analysis.

References

1 B. Fan, J. Yan and X. Yan, *Solid State Sci.*, 2011, **13**, 1835.
2 O. Yamamoto, *Electrochim. Acta*, 2000, **45**, 2423.
3 K. Kordesch and G. Simader, *Fuel Cells and Their Applications*, VCH, Weinheim/Wiley, NY, 1996.
4 K. Nagasawa, S. Daviero-Minaud, N. Preux, A. Rolle, P. Roussel, H. Nakatsugawa and O. Mentré, *Chem. Mater.*, 2009, **21**, 4738.
5 A. Rolle, S. Boulfrad, K. Nagasawa, H. Nakatsugawa, O. Mentré, J. Irvine and S. Daviero-Minaud, *J. Power Sources*, 2011, **196**, 7328.
6 A. Rolle, V. Thoréton, P. Rozier, E. Capoen, O. Mentré, B. Boukamp and S. Daviero-Minaud, *Fuel Cells*, 2012, **12**(2), 288.
7 A. J. Samson, M. Søgaard, N. Van Nong, N. Pryds and N. J. Bonanos, *J. Power Sources*, 2011, **196**, 10606.
8 J. Zou, J. Park, H. Yoon, T. Kim and J. Chung, *Int. J. Hydrogen Energy*, 2012, **37**, 8592.
9 H. B. Yahia, F. Mauvy and J. C. Grenier, *J. Solid State Chem.*, 2010, **183**, 527.
10 Y. H. Lin, C. W. Nan, Y. Liu, J. Li, T. Mizokawa and Z. Shen, *J. Am. Ceram. Soc.*, 2007, **90**, 132.
11 H. Muguerra, D. Grebille and F. Bourée, *Acta Crystallogr., Sect. B: Struct. Sci.*, 2008, **64**, 144.
12 C. D. Ling, K. Aivazian, S. Schmid and P. Jensen, *J. Solid State Chem.*, 2007, **180**, 1446.
13 Y. Li, M. W. Xu and J. B. Goodenough, *J. Power Sources*, 2012, **209**, 40.
14 R. J. Chater, S. Carter, J. A. Kilner and B. C. H. Steele, *Solid State Ionics*, 1992, **53–56**, 859.
15 I. Yasuda and T. Hikita, *J. Electrochem. Soc.*, 1994, **141**, 1268.
16 J. Crank, *The Mathematics of Diffusion*, Clarendon Press, Oxford, 2nd edn, 1975.
17 H. J. M. Bouwmeester, C. Song, J. Zhu, J. Yi, M. Van Sint Annaland and B. A. Boukamp, *Phys. Chem. Chem. Phys.*, 2009, **11**, 9640.
18 C. Y. Yoo, B. A. Boukamp and H. J. M. Bouwmeester, *J. Solid State Electrochem.*, 2011, **15**, 231.
19 J. A. Kilner, S. J. Skinner and H. Brongersma, *J. Solid State Electrochem.*, 2011, **15**, 861.
20 J. Rodriguez-Carvajal, *Physica B*, 1993, **192**, 55.
21 L. Karvonen, H. Yamauchi and M. Karppinen, *Chem. Mater.*, 2008, **20**, 7143.
22 J. A. Kilner, B. C. H. Steele and L. Ilkov, *Solid State Ionics*, 1984, **12**, 89.

23 C. Masset, C. Michel, A. Maignan, M. Hervieu, O. Toulemonde, F. Studer and B. Raveau, *Phys. Rev. B: Condens. Matter Mater. Phys.*, 2000, **62**, 166.
24 J. Sugiyama, J. H. Brewer, E. J. Ansaldo, H. Itahara, K. Dohmae, Y. Seno, C. Xia and T. Tani, *Phys. Rev. B: Condens. Matter Mater. Phys.*, 2003, **68**, 134423.
25 S. Muñoz and U. Anselmi-Tamburini, *J. Mater. Sci.*, 2010, **45**, 6528.
26 A. Atkinson, R. J. Chater and R. Rudkin, *Solid State Ionics*, 2001, **139**, 233.
27 R. Sayers, R. A. De Souza, J. A. Kilner and S. J. Skinner, *Solid State Ionics*, 2010, **181**, 386.
28 A. V. Berenov, A. Atkinson, J. A. Kilner, E. Bucher and W. Sitte, *Solid State Ionics*, 2010, **181**, 819.
29 A. Tarancón, S. J. Skinner, R. J. Chater, F. Hernández-Ramirez and J. A. Kilner, *J. Mater. Chem.*, 2007, **17**, 3175.
30 M. de Ridder, A. G. J. Vervoort, R. G. van Welzenis and H. H. Brongersma, *Solid State Ionics*, 2003, **156**, 255.
31 I. C. Fullarton, J. P. Jacobs, H. E. Benthem, J. A. Kilner, H. H. Brongersma, P. J. Scanlon and B. C. H. Steele, *Ionics*, 1995, **1**, 51.
32 M. M. Viitanen, R. G. van Welzenis, H. H. Brongersma and F. P. F. van Berkel, *Solid State Ionics*, 2002, **150**, 223.